Journal of Materials Chemistry A

Simple Transfer from Spin Coating to Blade Coating Through Processing Aggregated Solutions

Jeff L. Hernandez[‡], Nabankur Deb[‡], Rylan M.W. Wolfe[‡], Chi Kin Lo[‡], Sebastian Engmann[†], Lee J. Richter [†], and John R. Reynolds [*,‡]

‡ School of Chemistry and Biochemistry, School of Materials Science and Engineering, Center for Organic Photonics and Electronics, Georgia Tech Polymer Network, Georgia Institute of Technology, Atlanta, Georgia 30332, United States

† Material Measurement Laboratory, National Institute of Standards and Technology, Gaithersburg, Maryland 20899, United States

Abstract: To develop an understanding of the effect spin coating or blade coating have on the morphology of polymer:fullerene thin films for organic solar cells, we have investigated the morphology of poly[5-(2-hexyldecyl)-1,3-thieno[3,4-c]pyrrole-4,6-dione-alt-5,5-(2,5-bis(3-dodecylthiophen-2-yl)-thiophene)] (P(T3-TPD)) blended with phenyl-C71-butyric acid methyl ester ($PC_{71}BM$) using the solvent additive 1,8-diiodooctane (DIO). When P(T3-TPD):$PC_{71}BM$ mixtures are cast with DIO, we observed a fivefold increase in power conversion efficiency (PCE) from 1 % to >5 % for both spin and blade coated devices. We found the morphology and OPV performance are remarkably similar for spin and blade coated films without having to re-optimize the processing solution or coating temperature. We attribute the robust coating behavior to processing an aggregated solution of P(T3-TPD):$PC_{71}BM$. Further, in order to gain insight into how the common solvent additive DIO enhances thin film morphology, in situ UV-vis absorbance and reflection spectroscopies, coupled with thin film morphology characterization, was performed to develop a mechanistic understanding of the solidification process. In situ and static measurements revealed that DIO increases the nucleation density, reducing domain size and additionally increases the polymer crystallinity and phase purity.

Introduction:

As conjugated polymers used in bulk heterojunction (BHJ) solar cells continue to be developed and refined, many structurally dissimilar systems now exhibit AM 1.5G power conversion efficiencies (PCE) between 8% and 11%.[1-3] The material diversity presented in

laboratory scale devices drives a need for developing and understanding rules for scaling to large scale coating processes. Recent attention has brought up the importance of transitioning laboratory studies away from spin coating to roll-to-roll compatible processing methods, such as blade coating, spray coating, and slot die coating, that more properly mimic practical processing approaches and yield thin films with morphologies that match those that will be obtained in large scale production.[4,5,6] Within the multi-component processing solutions (inks) employed for polymer:fullerene,[7] polymer:non-fullerene acceptor,[8] and polymer:polymer blends,[9] the use of processing additives to enhance performance through morphology control has become wide-spread.[7, 10, 11] However, a clear understanding of both the influence that processing type has on morphology and the mechanisms of how these additives interact with the various components to form a more optimum phase separated morphology has not emerged.

A review of non-spun coat, small area devices found that,[4] as of 2013, in 36 trials only 4 systems demonstrated PCE greater than 4%, indicating the general complexity of using spin coating to guide scalable deposition.[12] Blade coating is an easily implemented prototyping tool[13] for direct comparison to continuous deposition processes such as slot-die coating.[14] With care, similar PCE can be attained between optimized spun coat and blade coat devices.[15-20] The transfer from spin coating to blade coating usually involves re-optimization of both the starting solution and deposition conditions, such as substrate temperature, in order to match the drying dynamics of spin coating.[21, 22] Zhao et al. found that simple transfer from spin coating to blade coating of PTB7, PTB7-Th, and PBDTTT-CT yielded decreased organic photovoltaic (OPV) performance for blade coated samples. A re-optimization was required that included tuning the solution solids content, processing at an elevated temperature and changing the additive concentration to maintain similar additive to solute volume ratio in order to mimic the drying kinetics of spin coating and achieve similar device performance and film morphology.[23] In contrast, recent work by Ro et al. showed that optimized blade coating of PffBT4T-2OD:$PC_{71}BM$, while yielding similar OPV performance to spin coating, not only required significant modification in coating conditions (substrate temperature) but produced significantly different film morphologies.[14]

In this study, we utilize the high performance, semi-crystalline polymer poly[5-(2-hexyldecyl)-1,3-thieno[3,4-c]pyrrole-4,6-dione-alt-5,5-(2,5-bis(3-dodecylthiophen-2-yl)-

thiophene)], P(T3-TPD), developed by Marks and co-workers,[24-26] to explore in detail the effect that ink formulation (presence of solution additive) and processing type (spin coating or blade coating) have on dry film morphology and OPV performance. P(T3-TPD) has been demonstrated to provide high power conversion efficiencies when processed via spin coating with $PC_{71}BM$ and the processing additive 1,8-diiodooctane (DIO),[24] and in polymer:polymer blends with the Polyera polymer N2200* when processed with the solvent additive 1-chloronapthalene.[26] We find no re-optimization of solution composition is necessary when transferring P(T3-TPD):$PC_{71}BM$ inks from spin coating to blade coating. We attribute this to processing from an aggregated solution that predetermines the solid-state morphology regardless of the processing method which is advantageous for the scaling of OPV technology. To gain further insight into how phase separated morphology is developed with the solvent additive DIO, and without DIO (w/o DIO), we perform in situ UV-vis absorbance and reflectance on blade coated films. In situ thin film measurements, coupled with ex situ film measurements, reveal that DIO increases the nucleation density during solidification, leading to reduced domain size and enhanced polymer crystallinity in the BHJ film.

Experimental

Organic solar cell fabrication. Patterned indium tin oxide (ITO) was sonicated in a solution of sodium dodecyl sulfate and Millipore water,* then rinsed with Millipore water, followed by sonication in acetone, then isopropanol for 5 minutes in each solvent. The ITO was blown dry with nitrogen gas, then UV ozone cleaned for 10 minutes. ZnO sol-gel[27] was spun coat onto the ITO at 84 rad s^{-1} (800 r.p.m.) for 50 s and then annealed at 300 °C for 5 min in air resulting in a 30 nm thick film. Solutions of P(T3-TPD):$PC_{71}BM$ (1:2 weight ratio), [12 mg mL^{-1}], in chloroform, or in chloroform:DIO (98 %:2 % by volume), were either blade coated onto the substrates in air with a blade to substrate gap of 300 μm and a blade velocity of ≈20 mm s^{-1} or spun coat at 314 rad s^{-1} (3000 r.p.m.) for 60 s in an Ar filled glovebox. Solutions were prepared by heating the ink to 50 ºC on a hotplate, then allowing it to cool to room temperature prior to film deposition. Films processed from chloroform without DIO were immediately placed in a thermal evaporator for contact deposition, while films processed from chloroform with 2% DIO

* Certain commercial equipment, instruments, or materials are identified in this paper in order to specify the experimental procedure adequately. Such identification is not intended to imply recommendation or endorsement by the National Institute of Standards and Technology, nor is it intended to imply that the materials or equipment identified are necessarily the best available for the purpose.

added by volume were allowed to dry 2 hours in ambient air for blade coated films, or in an Ar filled glovebox for spin coated films, prior to electrode deposition. Devices were placed in a thermal evaporator at a pressure of < 10^{-3} Pa for 1 hour prior to sequential deposition of 8 nm MoO_3 followed by 120 nm Ag which were used as the top electrodes. The active area of the devices, defined by the overlap of the top and bottom electrode, was 0.07 cm^2. Film thicknesses for blade coated devices were optimized to achieve the highest PCE and measured using a Bruker DetakXT profilometer. Devices were tested in an Ar filled glovebox using a Newport class ABB solar simulator coupled with a Keithley SMU 2410 for measuring device efficiency under standard AM 1.5G conditions calibrated to 95 mW cm^{-2}. A Newport EQE/IPCE setup with a Newport 66485 xenon lamp, an Oriel CS26 VIS-NIR 1/4 m monochromator, and a Merlin 70104 Digital Lock-in radiometry detector, were used.

X-ray Scattering: Grazing incidence wide angle X-ray scattering (GIWAXS) measurements were carried out on beamline 11-3 at the Stanford synchrotron radiation light source (SSRL). The beam energy was 12.7 keV. The angle of incidence was 0.12°, whereas the nominal critical angle for the films at the used energy is about 0.08°. A LaB_6 standard sample was used to calibrate the instrument and the software WxDiff[28] version 1.11 was used to reduce the 2-D scattering data into the corrected 1-D integration plots (I vs q and I vs chi). The sample to detector distance was ca. 400 mm. The crystalline correlation length (CCL) was estimated using $CCL = 2\pi/\Delta q_{FWHM}$, where Δq_{FWHM} is the full width half maximum of the (100) peak.[29] Grazing incidence small angle X-ray scattering (GISAXS) was also carried out at SSRL on beamline 1-5 with a beam energy of 10 keV and an incidence angle of 0.12°. The sample to detector distance was ca. 2900 mm. IGOR PRO with Nika,[30] and Irena, packages were used to reduce the GISAXS data.

Space Charge Limited Current (SCLC) Hole devices: ITO, cleaned in the same fashion as that used in solar cell devices, was coated with PEDOT:PSS (Clevios P VP Al 4083) filtered through a 0.45 µm nylon filter, by spin coating in air at 523 rad s^{-1} (5000 r.p.m.) for 60 s. Films were dried in ambient air on a hot plate at 120 °C for 10 min. A solution of P(T3-TPD):$PC_{71}BM$ (1:2 weight ratio), [12 mg mL^{-1}], was blade coated with a 500 µm gap at 30 mm s^{-1} to produce films that were 300 nm thick as measured using a Bruker DetakXT profilometer. Devices were

allowed to dry, followed by evaporation of 100 nm of Au. SCLC hole mobility was determined in the same way as reference [31].

Atomic force microscopy (**AFM)**: AFM was collected using a Bruker atomic force microscope (Dimension icon) with a Bruker Tap 150 cantilever in standard tapping mode.

In situ UV-vis measurement: In situ UV-Vis absorbance/reflection spectra were collected during deposition of films using optimized solar cell parameters. Solutions of P(T3-TPD):$PC_{71}BM$ (1:2 weight ratio [12 mg mL^{-1}] were coated on top of quartz that was cleaned with isopropanol, then UV ozone cleaned for 10 minutes. A fiber optic spectrometer based system (Dual spectrometer - Ocean Optics Inc. SD 2000) was used to simultaneously record s-polarized reflection and p-polarized transmission spectra at an incidence angle near the substrate's Brewster angle (≈ 56°). Polarizers were setup in front of the collection optics to select p-polarized light for the transmission and s-polarized light for the reflection and the incident light is non-polarized. The integration time for both the transmission and reflection channels was 50 ms, and the first available spectrum was collected after 50 ms and every 50 ms thereafter for further analysis.

Results and Discussion:

1.1 Solution Properties.

P(T3-TPD), having the repeat unit chemical structure shown in **Figure 1** a) and a number average molar mass (M_n) of 19.7 kDa, was synthesized according to a modified literature procedure (**Supporting Information, (SI)**). The polymer was found to be soluble in chloroform up to ~3 mg mL^{-1} at room temperature by passing a known amount of saturated solution through a 0.45 µm PTFE filter onto a pre-weighed glass slide and taking the mass difference upon solvent evaporation. The polymer was found to be insoluble in DIO at room temperature. **Figure 1** b) shows the temperature dependent UV-vis absorbance of P(T3-TPD) in chloroform indicating that it displays thermochromism in dilute solution (~ 0.1 mg mL^{-1}). At elevated temperature, the polymer is in a non-aggregated state and the solution appears orange, while at room temperature the polymer is aggregated and the solution appears purple. This observed thermochromic transition was found to be reversible with no hysteresis (**Figure S1, SI**). When the polymer is in a non-aggregated state at 50 ºC, its λ_{max} is at 480 nm. As the solution cools to room temperature, there is a planarization of the polymer backbone, extending the conjugation

length,[32] which causes the λ_{max} to shift to 580 nm, along with the development of a low energy shoulder at 635 nm. The longer wavelength absorbance is typically attributed to an increased aggregation of the polymer chains.[33] **Figure 1** c) shows the UV-vis absorbance spectra of the BHJ solution (solid line) and BHJ thin film (dashed line) normalized to the $PC_{71}BM$ peak at 375 nm with DIO and w/o DIO. The addition of DIO to a dilute (0.04 mg mL^{-1}) BHJ solution, seen in the UV-vis absorbance solution spectra in **Figure 1** c), shows a slight increase in absorbance intensity suggesting that DIO promotes additional aggregation. The BHJ thin film UV-vis absorbance, normalized to the $PC_{71}BM$ peak at 375 nm, also shown in **Figure 1** c), demonstrates that DIO significantly increases the polymer order in the dry film evidenced by the increase in optical absorbance of the low energy peaks, and a 20 nm red-shift in the λ_{max}. It is important to note that all thin films used in this study are processed at room temperature meaning that a solution of aggregates are being coated and not a well dissolved solution.

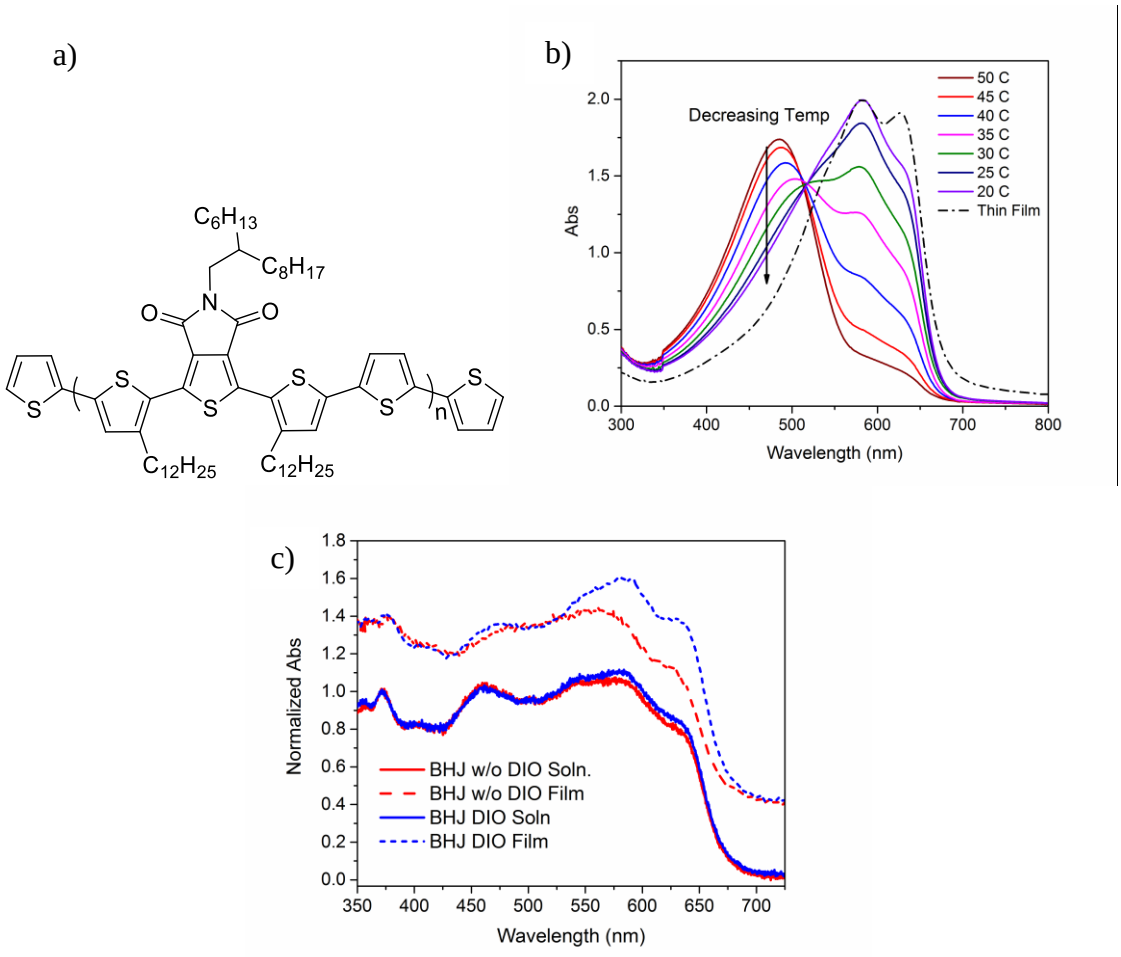

Figure 1. a) Repeat unit structure of P(T3-TPD), b) temperature dependent solution UV-vis absorbance spectra of neat P(T3-TPD) in chloroform and thin film UV-vis of neat P(T3-TPD). c) Comparison of spectra of the solution and dry film with DIO and w/o DIO. The solid lines show P(T3-TPD):$PC_{71}BM$ in chloroform with DIO and w/o DIO at 25°C. Dashed lines correspond to the UV-vis absorbance of BHJ thin film processed with DIO and w/o DIO. For clarity, the absorbance of the films with DIO and w/o DIO was offset by 0.4.

1.2 Photovoltaic Properties.

Bulk heterojunction OPV devices were processed at room temperature from chloroform, w/o DIO, or chloroform with 2% DIO added by volume, labeled as DIO, using an inverted solar cell architecture of ITO/ZnO/P(T3-TPD):$PC_{71}BM$ (1:2 weight ratio)/MoO_3/Ag. **Figure 2** a) shows the current-voltage characteristics (*J-V* curves) of devices made with DIO and w/o DIO processed using spin coating or blade coating demonstrating that the addition of a small amount of DIO has a pronounced effect on the solar cell electrical characteristics for both deposition techniques. **Table 1** shows the addition of DIO afforded a fivefold increase in short circuit current density (J_{sc}) and *PCE*, along with an increase in fill factor (*FF*) from 44% to 61% for blade coated samples. The large increase in short circuit current is represented in the external quantum efficiency (*EQE*) spectrum, **Figure 2** b), where the addition of DIO leads to a significant increase in photon conversion between 350 nm and 700 nm, whereas the films processed from chloroform alone show EQE values <20 % across the spectrum. The integral of EQE multiplied by the photon flux corresponding to AM 1.5G closely matches the experimentally determined J_{sc} (**Table S1, SI**). When blade coating is compared to spin coating, the photovoltaic characteristics are similar with comparable reproducibility. While spin coated samples were processed in an Ar filled glovebox, blade coated samples were processed in ambient air, indicating that this system is not sensitive to processing type or atmosphere, which is advantageous for large scale ambient processing. The optimized film thickness for BHJ films cast from chloroform was found to be ≈ 90 nm while the optimized thickness for BHJ films cast with DIO was found to be ≈ 150 nm. The observation that films processed with the solvent additive optimize at greater thickness suggests reduced recombination and improved transport. Interestingly, no further optimization was needed when transferring from spin coating to blade coating to produce similar OPV performance. The solution used for spin coated devices is the same solution used for blade coated devices and the processing temperature remained the same.

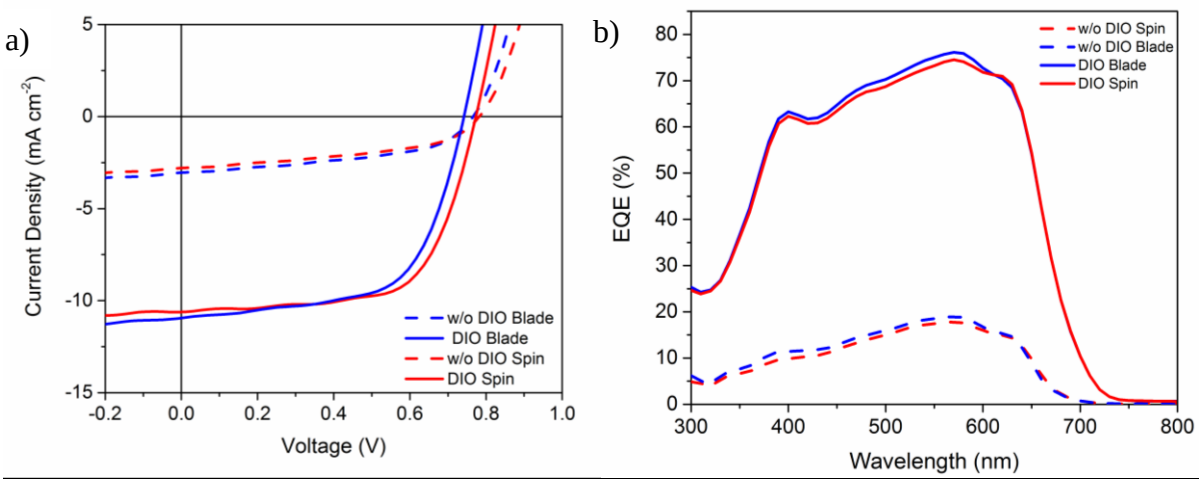

Figure 2. a) *J-V* characteristics of P(T3-TPD):$PC_{71}BM$ processed w/o DIO and with DIO, and processed via blade coating and spin coating. b) *EQE* of P(T3-TPD):$PC_{71}BM$ processed w/o DIO and with DIO via blade coating or spin coating.

Table 1. Comparison of solar cell electrical characteristics of P(T3-TPD):$PC_{71}BM$ processed w/o DIO or with DIO by blade coating or spin coating. Averaged values were obtained from 8 devices. Numbers in parenthesis represent best performing device.

Processing Condition	J_{sc} (mA/cm^2)	V_{oc} (V)	FF (%)	PCE (%)	Film Thickness (nm)
DIO (Blade)	11.5 ± 0.5 (11.8)	0.73 ± 0.01 (0.74)	61 ± 2 (61)	5.4 ± 0.1 (5.6)	150
w/o DIO (Blade)	2.7 ± 0.2 (3.0)	0.75 ± 0.02 (0.78)	44 ± 3 (48)	1.0 ± 0.1 (1.2)	90
DIO (Spin)	11.0 ± 0.5 (10.6)	0.74 ± 0.02 (0.76)	62 ± 3 (65)	5.3 ± 0.2 (5.5)	140
w/o DIO (Spin)	2.7 ± 0.2 (2.9)	0.75 ± 0.02 (0.78)	43 ± 3 (47)	0.9 ± 0.1 (1.1)	80

1.3 Thin Film Morphology

To elucidate the effect DIO has on P(T3-TPD):$PC_{71}BM$ BHJ thin film solidification, and to understand how this impacts solar cell performance, the morphology of dry spin coated and blade coated films was investigated. Atomic force microscopy (AFM) was used to qualitatively

probe the morphology of the BHJ system. Figure 3 depicts AFM height images of the BHJ film processed from the two solvent systems. Height images of the BHJ films processed w/o DIO show large features for both blade coated and spin coated films. The average feature diameter seen in blade coated samples is ≈280 nm, and in spin coated films is ≈260 nm which is in agreement with TEM images reported by Guo et al.[24] Evaluation of the topographic contrast demonstrates that the effect DIO has on polymer:fullerene phase separation is striking. Two key features stand out when examining the topographical contrast seen in the height images. First is how fine the phase separation is between polymer rich and fullerene rich phases. This observed reduction in feature size suggests an increased interfacial area between the polymer and fullerene, allowing for increased charge separation that would account for the large increase in J_{sc} seen in the photovoltaic parameters. Secondly, the small fibril like structures, which are not seen in the BHJ films processed w/o DIO, indicates there is a change in polymer order at the surface. This trend is seen in both spin and blade coated films signifying that processing of aggregated P(T3-TPD):$PC_{71}BM$ solutions yields similar surface topologies.

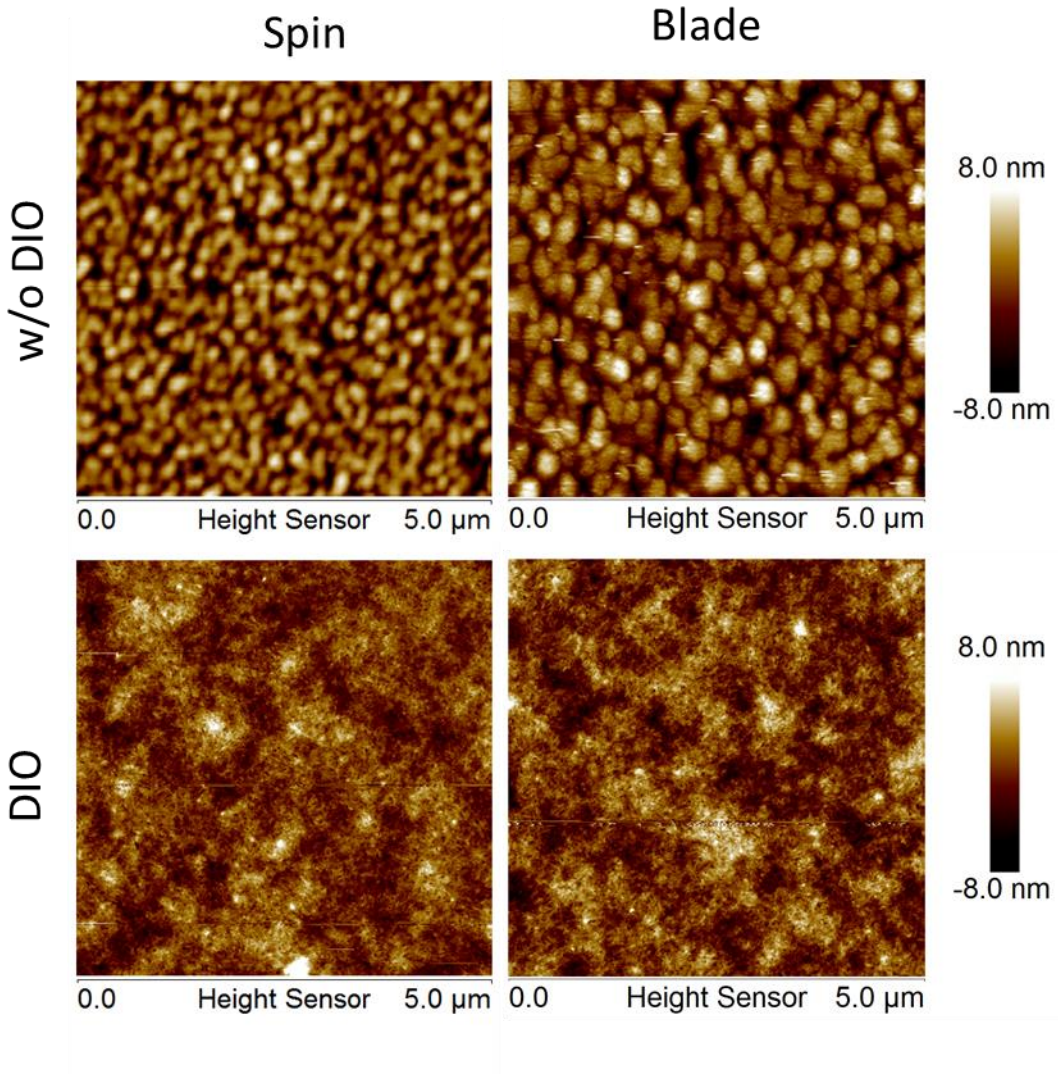

Figure 3. AFM height images of P(T3-TPD):$PC_{71}BM$ films processed by spin coating or by blade coating with DIO or w/o DIO. The image size in all cases is 5µm x 5µm.

Grazing incidence small angle X-ray scattering (GISAXS) was used to probe the bulk morphology of the BHJ films processed with DIO and w/o DIO. **Figure 4** shows log-log film thickness normalized GISAXS 1D line profiles at $q_z \approx 0$ of BHJ films processed using spin coating or blade coating both with DIO and w/o DIO. Films processed with DIO show a feature at scattering vectors q_{xy} of approximately 0.017 $Å^{-1}$ which corresponds to a domain spacing, calculated using $2\pi/q_{xy}$, of ca. 37 nm for both spin coated and blade coated films. The increase in scattering intensity seen in the films processed with DIO suggests enhanced domain purity, which is consistent with other high performance semi-crystalline polymer:fullerene systems.[1, 34]

The GISAXS of films processed without the solvent additive do not show a defined 'Guinier knee'[35] in the probed range indicating that the length scale is larger than 125 nm, consistent with the AFM. Remarkably, the BHJs processed using spin coating or blade coating show near identical characteristic length scales, in contrast to high performance systems such as PffBT4T-2OD,[14] and PBDT-TSR[36], which demonstrate different characteristic length scales based on deposition method.

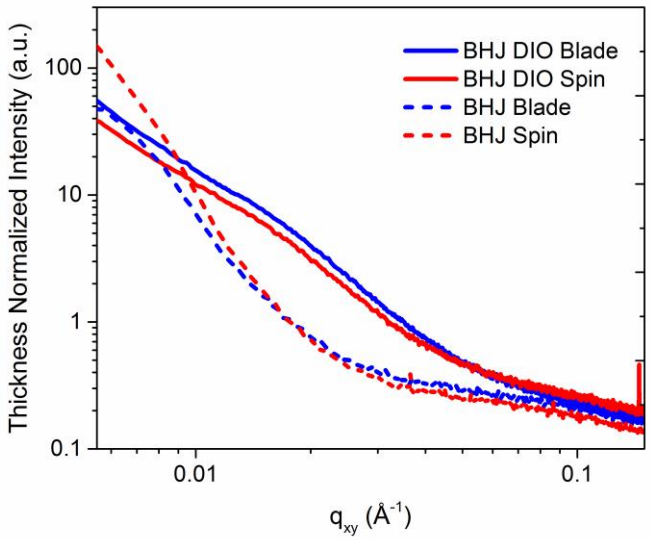

Figure 4. Thickness normalized GISAXS of BHJ films processed with DIO and w/o DIO using blade coating and spin coating.

In order to further understand the impact that processing type and additive have on polymer order, crystallinity, crystal orientation, and lamellar spacing, grazing incidence wide angle X-ray scattering (GIWAXS) was performed. **Figure 5** shows the film thickness and illumination time normalized (100) pole figures for spin coated, and blade coated, P(T3-TPD) and P(T3-TPD):$PC_{71}BM$ processed with DIO and w/o DIO extracted from 2D images (**Figure S2, SI**). Also shown in **Figure 5** (insets) is the relative degree of crystallinity (rDoC), calculated using $\int_0^{\frac{\pi}{2}} I(\chi) \sin\chi \, d\chi$,[37] for the different preparation conditions. From **Figure 5** a) it can be deduced that DIO has a twofold impact. First, it changes the polymer crystallite orientation from being bimodal (significant edge on and face on components, relative to the surface plane) to mostly face on when processed with DIO. This is evident from the loss of intensity centered around $\chi \approx$

0 º and increase in intensity near $\chi \approx \pm 90$ º. Secondly, DIO changes the rDoC. When the neat polymer is processed with the additive, DIO significantly suppresses crystallinity; however, in the BHJ films DIO slightly enhances polymer crystallinity. It is not uncommon to observe enhanced crystallinity in the BHJ films when a processing additive is used. This has been shown for multiple semi-crystalline polymer:fullerene blends. [7,14, 38] Examination of the blade coated films in **Figure 5** b) shows similar characteristics to that of the spin coated films. First, DIO influences crystal orientation. Again, when processed without the additive DIO the crystal orientation is bimodal as indicated by the strong intensity near $\chi \approx 0$ º and $\chi \approx \pm 90$ º. The addition of DIO drastically reduces the edge on orientation and increases the face on crystal orientation analogous to spin coated films. Like the spin coated samples, the addition of DIO suppresses polymer crystallization in the neat sample. However, it enhances polymer crystallization in the BHJ samples. In both the spin coated and blade coated BHJ films we find that DIO enhances polymer crystallinity, changes the crystal orientation, and reduces domain size. The reduction in feature size found in the AFM images coupled with the enhanced polymer crystallinity in the BHJ films, shown in the GIWAXS, signals that DIO serves to increase nucleation density.

Like the results observed in the AFM and GISAXS both spin coating and blade coating of the aggregated solution yield very similar GIWAXS characteristics. The lamellar stacking distance, and π-π stacking distance (**Table S2, SI**) were found to be similar for blade coated and spin coated films. In fact, the only observed difference between the two processing methods is the crystal coherence length (CCL), which was found to be larger for spin coated samples relative to blade coated samples. The difference in CCL found in spin and blade coated P(T3-TPD):$PC_{71}BM$ samples indicate that a range of crystal dimensions achieves similar device performance.

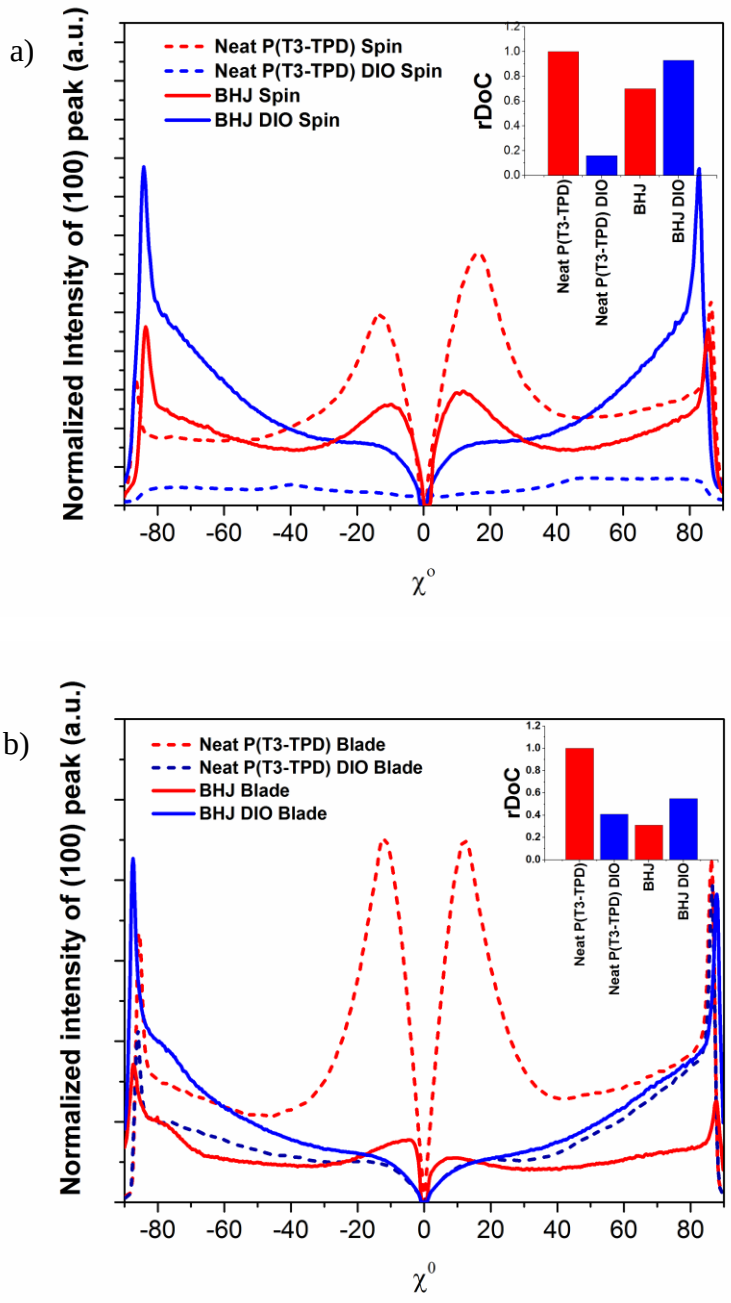

Figure 5. Thickness and illumination time normalized, sin χ corrected pole figures of a) spin coated, and b) blade coated, neat P(T3-TPD) films and BHJ films each processed with DIO and w/o DIO. For BHJ samples the polymer volume fraction was taken into account.

1.4 Hole Mobility

Space charge limited current (SCLC) measurements were performed in order to investigate whether or not the crystal orientation change from bimodal to preferentially face on contributes to increased mobility through the device, which could be the cause of the observed increase in short circuit current density. For some conjugated systems it is hypothesized that face on orientation of crystallites is beneficial for charge carrier transport to the electrodes for solar cells.[39, 40] Using a modified Mott-Gurney expression,[31] SCLC hole mobility was found to be $(1.1\pm0.4)\times10^{-4}$ cm^2 V^{-1} s^{-1} and $(2.1\pm1.2)\times10^{-4}$ cm^2 V^{-1} s^{-1} for 300 nm thick blade coated BHJ films cast w/o DIO and with DIO respectively with the deviation accounting for fit uncertainty. (**Figure S3, SI)** While the addition of DIO changes the edge-on to face-on ratio, this does not appear to have a significant impact on charge transport. Therefore, the impact of crystal orientation with respect to the substrate seen in BHJ films processed with DIO is insufficient for explaining the large increase in J_{sc} when DIO is used as a solvent additive.

Spin coating and blade coating the same concentration solution at room temperature results in nominally identical device performance and behavior at optimal thickness w/o DIO and with DIO. This is consistent with the production of virtually identical film morphology by all measures, which is striking, given the radically different drying speeds of spin coating and blade coating.[21] We ascribe this observed similarity to the use of an aggregated solution that appears to dominate the final film morphology with respect to drying dynamics.

1.5 In situ UV-vis and Morphology Evolution:

In situ morphology evolution studies have proven to be a powerful method for investigating thin film solidification of polymer:fullerene blends cast from mixed solvents. [27, 41-45] In an attempt to gain insight into how DIO influences the BHJ film formation, in situ reflection/absorbance UV-vis spectroscopy was performed during blade coating of P(T3-TPD):$PC_{71}BM$ films cast w/o DIO and with DIO. Polarized UV-vis absorbance spectroscopy of dry films was taken, in order to investigate in-plane optical anisotropy caused by a preferential orientation of the polymer backbone with respect to the blade coating direction in P(T3-TPD):$PC_{71}BM$; however, an in-plane orientation was not observed indicating that blade coating does not induce polymer alignment with respect to the blading direction in this system. (**Figure**

S4, SI). **Figure 6** shows both in situ absorbance and in situ reflection measurements taken at the same spot, at the same time, and on the same sample. 2D plots were rendered with the y-axis accounting for time (s), the x-axis for wavelength (nm), and the color represents absorbance, where a strong absorbance is yellow, and where there is little absorbance, dark blue. The passage of the blade was set to one second in order to compare time scales between films cast w/o DIO or with DIO. Films cast w/o DIO are straightforward, wherein the chloroform rapidly evaporates, and at approximately 3.5 s after blade passage the film is subsequently dry. The in situ UV-vis absorbance shows little evidence for formation of new aggregate peaks unlike P3HT:PCBM film solidification;[27, 46] however, by plotting the absorbance and reflection intensity as a function of time (**Figure S5 a, SI**) a subtle transition can be observed at ~2.5-3 s that suggests further aggregation of the polymer as concentration sharply increases during solidification. The most significant change in the UV-Vis upon film formation is a broad increase in absorbance above 400 nm, that we attribute to scatter due to film roughness and/or the coarse morphology. Films cast with DIO exhibit a two step drying process, and significantly increased drying times. Two transitions can be observed in the reflection spectra, the first one corresponds to the end of rapid chloroform evaporation at approximately 2.5 s after blade passage (**Figure S5 b, SI**), and the second transition is at the end of the DIO evaporation, that is not complete until ~5500 s. Both transitions seen in the in situ reflectance are marked by dashed lines and labeled in **Figure 6**. While the chloroform evaporation rate is rapid (<4 s), the complete evaporation rate of DIO is prolonged (~90 minutes). The evaporation of chloroform leaves a DIO swollen film in which the fullerene is soluble, but not the polymer. The extremely rapid evaporation of the chloroform precludes resolution of the expected interference fringes in the reflection data. Nonetheless, an inflection in the reflection can be observed at the anticipated point of chloroform removal and the radical slowing of the evaporation rate. The absorbance data, recorded at nominally Brewster's angle, are insensitive to the film thickness interference and directly probes the polymer backbone order. There is a distinct change upon removal of the chloroform. Interestingly, over the next 90 minutes, while evaporation of the DIO is clearly occurring as seen in the evolution of the reflection data, there is little detectable change in the absorbance spectra. As the transition dipole moment along the backbone is only sensitive to a planarization of the polymer backbone and aggregation, rather than a change in final crystallinity, invariant UV-vis absorbance does not omit the evolution of higher order, such as crystallinity. Similar invariant

UV-vis spectra were reported during the processing of P3HT with the non-solvent octane dithiol.[38] In order to gain more quantitative insight into the time resolved absorbance spectra, three features, P1-P3, as labeled in **Figure 6** were deconvoluted into three Gaussian peaks. The FWHM (σ) and the height (H) of the Gaussian peaks were plotted as a function of time in order to investigate if any changes had occurred during solvent evaporation as seen in **Figure S6, SI**. It was found that when using an aggregated solution of P(T3-TPD):$PC_{71}BM$ there are no significant changes in polymer aggregation that occur, other than increased aggregation during solidification, that were detected using in situ UV-vis absorbance. This further reinforces that an aggregated solution is being processed, and suggests that film morphology is predetermined when processing polymer aggregates and is less sensitive to processing method.

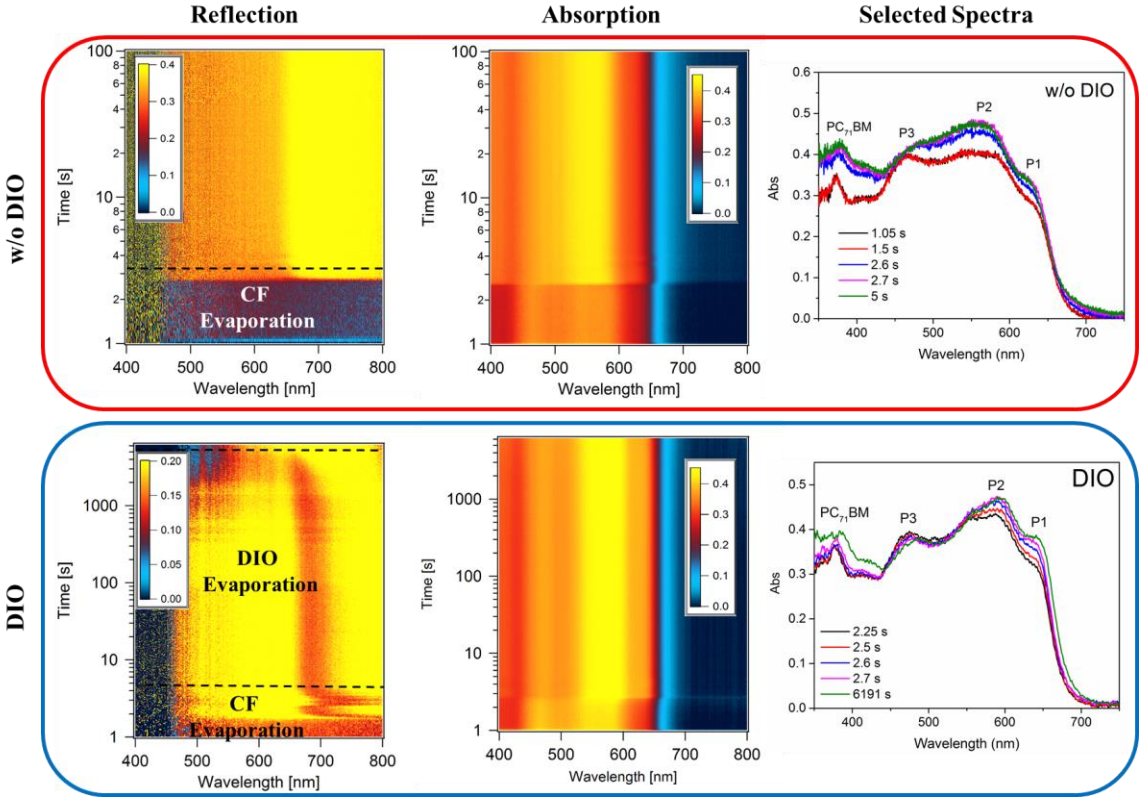

Figure 6. In situ reflection/absorbance UV-Vis measurements of blade coated pre-aggregated P(T3-TPD):$PC_{71}BM$ films cast with DIO and w/o DIO. Time resolved absorbance spectra were selected to show there is little change in local order during solidification.

Combining the morphology and kinetic studies, a coherent picture of the processing of P(T3-TPD):$PC_{71}BM$ emerges. The robust behavior with respect to coating method: nominally identical

film morphology and device performance is obtained with the same solution at the same temperature for both spin and blade coating, is directly attributable to the high level of aggregation in the solution. However, the overall low solids content enables adequate film quality for good devices, which is often not observed when processing from aggregated solutions.[14] While solution aggregates are critical for OPV[47] and OFET[48] performance, it is also clear that the presence of DIO in the solution significantly modifies the final film characteristics. The decrease in characteristic dimension for phase separation is consistent with the observation that DIO is a non-solvent for P(T3-TPD). It thus will lower the processing solution solvent quality, increasing the enthalpic drive for aggregation, increasing the nucleation density. An interesting question arises as to the origin of the beneficial effect of DIO on order and phase purity. Changes in nucleation density do not directly relate to subsequent changes in crystal growth and quality. Based on the in situ UV-vis absorbance and reflectance, the dominant effect of DIO on aggregation occurs during the early stages of deposition, consistent with the deposition of aggregates. However, it is possible that simply extending the time over which the film is swollen with DIO (90 min) provides an opportunity for increased crystallization. Additionally, the selective solvent nature of DIO can plasticize any mixed amorphous phases of P(T3-TPD) and PCBM and extract the fullerene.[38, 49]

Conclusion:

Using P(T3-TPD):$PC_{71}BM$, we have shown that processing via spin coating or blade coating yields similar electrical and morphological characteristics when processed from an aggregated solution. This is quite contrary to other polymer:fullerene systems which show drastic differences in film morphology and solar cell performance when processed via spin coating or blade coating. We have investigated the impact that DIO has on BHJ thin film morphology development. Using AFM, GIWAXS, and GISAXS, we show that DIO enhances the crystallinity of the polymer and reduces the domain size in the BHJ film. The decreased domain size increases the polymer:fullerene surface area which enhances the short circuit current density, and improves OPV performance. Combining static thin film measurements with in situ UV vis absorbance and reflectance spectroscopy reveal that DIO serves to increase the nucleation density which in turn reduces the average domain size and enhances polymer crystallinity. The lack of solution re-optimization, and simple transfer from spin coating to blade

coating, without impacting the BHJ morphology, by using aggregated solutions, is advantageous for the scale up of organic electronic devices via roll-to-roll processing. The use of aggregated solutions opens the door to move away from traditional spin coating to more scalable processing methods for organic electronics without undertaking extensive reoptimization studies. Broadly speaking, we show the use of aggregated polymer solutions pins the resultant thin film morphology regardless of processing method.

Acknowledgements: We acknowledge funding of this work from the Office of Naval Research (N00014-17-1-2243). R. Wolfe acknowledges support from the DoD's National Defense Science and Engineering Graduate (NDSEG) Fellowship, 32 CFR 168a. Jeff Hernandez thanks the NSF NESAC IGERT (DGE-1069138) program for Traineeship support. The authors acknowledge Chris Tassone from SSRL for aid in GIWAXS/GISAXS setup and data processing.

References:

1. Y. Liu, J. Zhao, Z. Li, C. Mu, W. Ma, H. Hu, K. Jiang, H. Lin, H. Ade and H. Yan, *Nature communications*, 2014, **5**, 5293.
2. Z. He, B. Xiao, F. Liu, H. Wu, Y. Yang, S. Xiao, C. Wang, T. P. Russell and Y. Cao, *Nature Photonics*, 2015, **9**, 174-179.
3. J. Zhao, Y. Li, G. Yang, K. Jiang, H. Lin, H. Ade, W. Ma and H. Yan, *Nature Energy*, 2016, **1**, 15027.
4. M. Hösel, H. F. Dam and F. C. Krebs, *Energy Technology*, 2015, **3**, 293-304.
5. X. Gu, Y. Zhou, K. Gu, T. Kurosawa, Y. Guo, Y. Li, H. Lin, B. C. Schroeder, H. Yan and F. Molina-Lopez, *Advanced Energy Materials*, 2017, 1602742.
6. Y. Lin, C. Cai, Y. Zhang, W. Zheng, J. Yang, E. Wang and L. Hou, *Journal of Materials Chemistry A*, 2017, **5**, 4093-4102.
7. H.-C. Liao, C.-C. Ho, C.-Y. Chang, M.-H. Jao, S. B. Darling and W.-F. Su, *Materials today*, 2013, **16**, 326-336.
8. Y. Sun, G. C. Welch, W. L. Leong, C. J. Takacs, G. C. Bazan and A. J. Heeger, *Nature materials*, 2012, **11**, 44-48.
9. Y.-J. Hwang, T. Earmme, B. A. Courtright, F. N. Eberle and S. A. Jenekhe, *Journal of the American Chemical Society*, 2015, **137**, 4424-4434.
10. J. K. Lee, W. L. Ma, C. J. Brabec, J. Yuen, J. S. Moon, J. Y. Kim, K. Lee, G. C. Bazan and A. J. Heeger, *Journal of the American Chemical Society*, 2008, **130**, 3619-3623.
11. W. Zhao, L. Ye, S. Zhang, M. Sun and J. Hou, *Journal of Materials Chemistry A*, 2015, **3**, 12723-12729.
12. R. G. Brandt, F. Zhang, T. R. Andersen, D. Angmo, M. Shi, L. Gurevich, F. C. Krebs, J. W. Andreasen and D. Yu, *RSC Advances*, 2016, **6**, 41542-41550.
13. C. M. Stafford, K. E. Roskov, T. H. Epps III and M. J. Fasolka, *Review of scientific instruments*, 2006, **77**, 023908.

14. H. W. Ro, J. M. Downing, S. Engmann, A. A. Herzing, D. M. DeLongchamp, L. J. Richter, S. Mukherjee, H. Ade, M. Abdelsamie and L. K. Jagadamma, *Energy & Environmental Science*, 2016, **9**, 2835-2846.
15. Y.-H. Chang, S.-R. Tseng, C.-Y. Chen, H.-F. Meng, E.-C. Chen, S.-F. Horng and C.-S. Hsu, *Organic Electronics*, 2009, **10**, 741-746.
16. P. Schilinsky, C. Waldauf and C. J. Brabec, *Advanced Functional Materials*, 2006, **16**, 1669-1672.
17. S.-L. Lim, E.-C. Chen, C.-Y. Chen, K.-H. Ong, Z.-K. Chen and H.-F. Meng, *Solar Energy Materials and Solar Cells*, 2012, **107**, 292-297.
18. P.-T. Tsai, C.-Y. Tsai, C.-M. Wang, Y.-F. Chang, H.-F. Meng, Z.-K. Chen, H.-W. Lin, H.-W. Zan, S.-F. Horng and Y.-C. Lai, *Organic Electronics*, 2014, **15**, 893-903.
19. J.-H. Chang, Y.-H. Chen, H.-W. Lin, Y.-T. Lin, H.-F. Meng and E.-C. Chen, *Organic Electronics*, 2012, **13**, 705-709.
20. M. Guérette, A. Najari, J. Maltais, J. R. Pouliot, S. Dufresne, M. Simoneau, S. Besner, P. Charest and M. Leclerc, *Advanced Energy Materials*, 2016, **6**, 1502094.
21. K. Xiong, L. Hou, M. Wu, Y. Huo, W. Mo, Y. Yuan, S. Sun, W. Xu and E. Wang, *Solar Energy Materials and Solar Cells*, 2015, **132**, 252-259.
22. J. J. van Franeker, S. Kouijzer, X. Lou, M. Turbiez, M. M. Wienk and R. A. Janssen, *Advanced Energy Materials*, 2015, **5,** 1500464.
23. K. Zhao, H. Hu, E. Spada, L. Jagadamma, B. Yan, M. Abdelsamie, Y. Yang, L. Yu, R. Munir and R. Li, *Journal of Materials Chemistry A*, 2016, **4**, 16036-16046.
24. X. Guo, N. Zhou, S. J. Lou, J. Smith, D. B. Tice, J. W. Hennek, R. P. Ortiz, J. T. L. Navarrete, S. Li, J. Strzalka, L.X. Chen, R.P.H. Chang, A. Facchetti, and T.J. Marks, *Nature Photonics*, 2013, **7**, 825-833.
25. N. Zhou, X. Guo, R. P. Ortiz, T. Harschneck, E. F. Manley, S. J. Lou, P. E. Hartnett, X. Yu, N. E. Horwitz, P. M. Burrezo, T.J. Aldrich, J.T. Lopez Navarrete, M.R. Wasielewski, L.X. Chen, R.P.H. Chang, A. Facchetti, and T.J. Marks, *Journal of the American Chemical Society*, 2015, **137**, 12565-12579.
26. N. Zhou, A. S. Dudnik, T. I. Li, E. F. Manley, T. J. Aldrich, P. Guo, H.-C. Liao, Z. Chen, L. X. Chen, R. P. H. Chang, A. Facchetti, M. Olvera de la Cruz, and T.J. Marks, *Journal of the American Chemical Society*, 2016, **138**, 1240-1251.
27. J. L. Hernandez, E. Reichmanis and J. R. Reynolds, *Organic Electronics*, 2015, **25**, 57-65.
28. S. Mannsfeld, *Stanford Synchrotron Radiation Lighsource*, 2009.
29. J. T. Rogers, K. Schmidt, M. F. Toney, G. C. Bazan and E. J. Kramer, *Journal of the American Chemical Society*, 2012, **134**, 2884-2887.
30. J. Ilavsky, *Journal of Applied Crystallography*, 2012, **45**, 324-328.
31. T. Ameri, P. Khoram, T. Heumüller, D. Baran, F. Machui, A. Troeger, V. Sgobba, D. M. Guldi, M. Halik and S. Rathgeber, *Journal of Materials Chemistry A*, 2014, **2**, 19461-19472.
32. H. F. Mark, *Encyclopedia of polymer science and technology, concise*, John Wiley & Sons, 2013.
33. T.-Q. Nguyen, V. Doan and B. J. Schwartz, *The Journal of chemical physics*, 1999, **110**, 4068-4078.
34. A. C. Stuart, J. R. Tumbleston, H. Zhou, W. Li, S. Liu, H. Ade and W. You, *Journal of the American Chemical Society*, 2013, **135**, 1806-1815.

35. J. C. Rivière and S. Myhra, *Handbook of surface and interface analysis: methods for problem-solving*, CRC press, 2009.
36. L. Ye, Y. Xiong, H. Yao, A. Gadisa, H. Zhang, S. Li, M. Ghasemi, N. Balar, A. Hunt and B. T. O'Connor, *Chemistry of Materials*, 2016, **28**, 7451-7458.
37. J. Rivnay, S. C. Mannsfeld, C. E. Miller, A. Salleo and M. F. Toney, *Chemical Reviews*, 2012, **112**, 5488-5519.
38. L. J. Richter, D. M. DeLongchamp, F. A. Bokel, S. Engmann, K. W. Chou, A. Amassian, E. Schaible and A. Hexemer, *Advanced Energy Materials*, 2015, **5**, 1400975.
39. I. Osaka, M. Saito, T. Koganezawa and K. Takimiya, *Advanced Materials*, 2014, **26**, 331-338.
40. C. Lu, H.-C. Chen, W.-T. Chuang, Y.-H. Hsu, W.-C. Chen and P.-T. Chou, *Chemistry of Materials*, 2015, **27**, 6837-6847.
41. B. Schmidt-Hansberg, M. Sanyal, M. F. Klein, M. Pfaff, N. Schnabel, S. Jaiser, A. Vorobiev, E. Müller, A. Colsmann and P. Scharfer, *Acs Nano*, 2011, **5**, 8579-8590.
42. F. Liu, Y. Gu, C. Wang, W. Zhao, D. Chen, A. L. Briseno and T. P. Russell, *Advanced Materials*, 2012, **24**, 3947-3951.
43. J. J. van Franeker, M. Turbiez, W. Li, M. M. Wienk and R. A. Janssen, *Nature communications*, 2015, **6**, 6229.
44. F. Liu, S. Ferdous, E. Schaible, A. Hexemer, M. Church, X. Ding, C. Wang and T. P. Russell, *Advanced Materials*, 2015, **27**, 886-891.
45. N. K. Zawacka, T. R. Andersen, J. W. Andreasen, L. H. Rossander, H. F. Dam, M. Jørgensen and F. C. Krebs, *Journal of Materials Chemistry A*, 2014, **2**, 18644-18654.
46. N. Shin, L. J. Richter, A. A. Herzing, R. J. Kline and D. M. DeLongchamp, *Advanced Energy Materials*, 2013, **3**, 938-948.
47. J. A. Bartelt, J. D. Douglas, W. R. Mateker, A. E. Labban, C. J. Tassone, M. F. Toney, J. M. Fréchet, P. M. Beaujuge and M. D. McGehee, *Advanced Energy Materials*, 2014, **4**, 1301733.
48. P.-H. Chu, N. Kleinhenz, N. Persson, M. McBride, J. L. Hernandez, B. Fu, G. Zhang and E. Reichmanis, *Chemistry of Materials*, 2016, **28**, 9099-9109.
49. D. Leman, M. A. Kelly, S. Ness, S. Engmann, A. Herzing, C. Snyder, H. W. Ro, R. J. Kline, D. M. DeLongchamp and L. J. Richter, *Macromolecules*, 2015, **48**, 383-392.

Graphical Abstract: